The Astrophysical Journal, 671:571–580, 2007 December 10

THE OUTFLOW FROM THE LUMINOUS YOUNG STELLAR OBJECT IRAS 20126+4104: FROM 4000 AU TO 0.4 pc

Yu-Nung Su and Sheng-Yuan Liu
Institute of Astronomy and Astrophysics, Academia Sinica, P.O. Box 23-141, Taipei 106, Taiwan; ynsu@asiaa.sinica.edu.tw

Huei-Ru Chen
Institute of Astronomy and Department of Physics, National Tsing Hua University, Hsinchu, Taiwan

Qizhou Zhang
Harvard-Smithsonian Center for Astrophysics, 60 Garden Street, Cambridge, MA 02138

and

Riccardo Cesaroni
Osservatorio Astrofisico di Arcetri, INAF, Largo E. Fermi 5, 50125 Firenze, Italy
Received 2007 July 5; accepted 2007 August 30

ABSTRACT

We have imaged the outflow from the luminous young stellar object IRAS 20126+4104 (I20126) with the Submillimeter Array in CO (3–2), HCN (4–3), and SiO (5–4) at 1″–2″ resolutions within a radius of ∼20″ from the central driving source. Our observations reveal at least three different components of the outflowing gas: (1) A compact (∼4000 AU) bipolar outflow toward the central young stellar object. With a dynamical timescale of ∼120 yr, this component represents a very new jet/outflow activity in I20126. (2) A collimated outflow with an extent of ∼0.2 pc previously detected in SiO (2–1). Both morphology and kinematics favor this component being a jet-driven bow shock system. (3) An S-shaped CO outflow with an extent of ∼0.4 pc. This component records the precession history very well. Its kinematic feature, where the velocity increases with distance from the YSO, indicates, independently of other evidence, that the outflow axis is moving toward the plane of the sky. The three outflow components record the history of the primary jet precession over scales ranging from a few hundred AU to approximately 0.4 pc. Our results indicate that CO (3–2) emission is a good tracer to probe the primary jet. The gas densities and SiO relative abundances in I20126 shocks are estimated using the large velocity gradient calculations. The inferred SiO abundances of (1–5) × 10^{-8} in I20126 outflow lobes are comparable to the expected enhancement at shocked regions.

Subject headings: H II regions — ISM: clouds — ISM: individual (IRAS 20126+4104) — stars: formation

1. INTRODUCTION

Bipolar molecular outflows are a magnificent phenomenon commonly identified around both low- and high-mass young stellar objects (YSOs; e.g., Bachiller & Tafalla 1999; Arce et al. 2007). It is, however, not clear how the bulk of the outflowing gas is accelerated. Observationally, molecular outflows in several cases can be divided into two components—the "classical" less-collimated component with low-velocity gas, and the highly collimated component with extremely high velocity (50–150 km s^{-1}) gas (Bachiller & Tafalla 1999; Hirano et al. 2006; Palau et al. 2006). That the outflow mass spectrum [$m(v) \propto v^{-\gamma}$] often has a broken power law, with the slope steepening at outflow velocities $v_{\rm flow} \gtrsim$ 10 km s^{-1} (e.g., Su et al. 2004), further indicates different characters between high- and low-velocity gas. A number of theoretical models have been proposed to interpret observed outflow features such as their morphology, kinematics, and energetics. These models can be divided into four types: (1) jet-driven bow shock models, (2) wind-driven-shell models, (3) turbulent flows, and (4) circulation models. The first two types are likely more promising, although no single type of model can reproduce the rich characteristics of observed outflows (for recent reviews, see Bachiller & Tafalla 1999; Arce et al. 2007).

At a kinematic distance of ∼1.7 kpc, IRAS 20126+4104 (hereafter I20126) is a nearby high-mass star-forming region with a far-IR luminosity of $\sim 10^4\,L_\odot$ and colors typical of ultracompact H II regions (Wood & Churchwell 1989). An outflow/jet system is clearly identified toward I20126 in a variety of tracers. Within approximately 10″ of the central YSO, a well-collimated outflow/jet at a position angle (P.A.) of ∼120° was revealed in SiO (2–1), HCO^+ (1–0), CH_3OH (2–1), CO (7–6), NH_3 (3, 3), and near-IR H_2 emission (Cesaroni et al. 1997, 1999, 2005; Kawamura et al. 1999; Zhang et al. 1999; Shepherd et al. 2000). Furthermore, this jet can be traced down to a linear scale of a few hundred AU through water maser emission and 3.6 cm emission from ionized gas (Hofner et al. 1999; Tofani et al. 1995; Moscadelli et al. 2000). Recently, multiepoch *VLBI* observations indicated that the water maser spots were expanding at speeds of ∼35–110 km s^{-1} from a common origin, i.e., the location of the YSO (Moscadelli et al. 2005). On large scales, a north-south molecular outflow with an extent of ∼2′ was detected in CO (1–0) (Shepherd et al. 2000). Near-IR observations in H_2 and [S II] also revealed several shock-excited knots spread in a region of ∼2′ (Shepherd et al. 2000). These knots displayed an S-shaped symmetry around the central young star. The innermost knots lie along the axis of the well-collimated outflow, while the outer knots are aligned roughly in the north-south direction. The different outflow orientations in the large and small scales were attributed to the outflow precession, and the S-shaped distribution of the shock-excited knots was argued as recording the precession history (Shepherd et al. 2000; Cesaroni et al. 2005).

A detailed study of the kinematics and morphology of molecular outflows at high spatial resolutions can provide essential clues for understanding the processes of acceleration. The association

TABLE 1
IRAS 20126+4104 Observational Parameters

Parameter	230 GHz Band	345 GHz Band
Number of antennas	8	6
Primary beam HPBW (arcsec)	~55	~35
Main lines	SiO (5–4)	CO (3–2)
		HCN (4–3)
Phase center α (J2000.0)	20 14 26.00	20 14 26.02
Phase center δ (J2000.0)	41 13 31.50	41 13 32.75
Projected baseline range (kλ)	16–150	15–80
Channel spacing (MHz/km s^{-1})	0.8125/1.1	0.8125/0.7
rms noise level[a] (mJy beam^{-1})	25 (0.51 K)	70 (0.27 K)
Synthesized beam size[b]	$1.4'' \times 0.9''$ (P.A. = 80.4°)	$1.8'' \times 1.5''$ (P.A. = −33.3°)
Gain calibrator	BL Lac and 2015+371	MWC 349 and BL Lac
Flux calibrator	Titan	Uranus
Passband calibrator	3C 279	3C 454.3

Note.—Units of right ascension are hours, minutes, and seconds, and units of declination are degrees, arcminutes, and arcseconds.
[a] In a 2 km s^{-1} velocity bin.
[b] Natural weighting at 230 GHz and robust weighting at 345 GHz.

with both "classical" and collimated outflows makes I20126 one of the best targets for such a study. We have carried out high-resolution (~1.5″, corresponding to ~2500 AU at a distance of 1.7 kpc) millimeter and submillimeter observations with the Submillimeter Array[1] (SMA) in SiO (5–4), CO (3–2), and HCN (4–3) transitions. This paper focuses on the results related to the morphology and kinematics of the outflow. We identify an extremely young and compact outflow, a jet-driven bow shock system, and an S-shaped outflow. These components are likely related to the primary jet. The physical conditions in I20126 shocks are also derived. Because I20126 is associated with a hot molecular core, an active outflow, and highly excited shocked components, a large number of transitions were also detected within the broad 4 GHz spectral coverage of the SMA. The detections of many species allow us to further study the chemistry in massive star-forming regions, and the results will be presented in another paper (i.e., S.-Y. Liu et al. 2008, in preparation).

2. OBSERVATIONS AND DATA REDUCTION

The observations were carried out with the SMA on 2004 August 25 and 2005 August 5. We observed SiO (5–4) in the 230 GHz (1.3 mm) band with eight antennas in the extended configuration, with projected baselines ranging from approximately 23 to 210 m (16–150 kλ). At the 345 GHz (0.85 mm) band, CO (3–2) and HCN (4–3) were simultaneously observed with six antennas in the compact configuration, with projected baselines ranging from about 13 to 70 m (15–80 kλ). The half-power width of the SMA primary beam was ~55″ at 217 GHz and ~35″ at 345 GHz. The total available double-sideband bandwidth was 4 GHz. See Ho et al. (2004) for more complete specifications of the SMA. The spectral resolution was 0.8125 MHz, corresponding to a velocity resolution of ~1.1/0.7 km s^{-1} at 217/345 GHz. For the 230 GHz band, the absolute flux density scales were determined from observations of Titan, and the bright quasar 3C 279 was used for bandpass calibration. To calibrate relative amplitude and phase, we observed a pair of nearby compact radio sources, 2202+422 (also known as BL Lac) and 2015+371. For the 345 GHz band, Uranus and 3C 454.3 were used for flux and bandpass calibration, respectively, and a pair of nearby compact radio sources, MWC 349 and BL Lac, were used for amplitude and phase calibration. We calibrated the data using the MIR software package adapted for the SMA from the software package developed originally for the OVRO MMA (Scoville et al. 1993). We made maps using the MIRIAD package. The synthesized beam size was about $1.4'' \times 0.9''$ with natural weighting at 217 GHz and approximately $1.8'' \times 1.5''$ with robust weighting at 345 GHz. We smoothed our data to 2.0 km s^{-1} resolution for the analysis presented below. The rms noise level in a 2.0 km s^{-1} velocity bin was ~25 mJy beam^{-1} at 217 GHz and ~70 mJy beam^{-1} at 345 GHz. Details of the observation parameters are listed in Table 1.

[1] The Submillimeter Array is a joint project between the Smithsonian Astrophysical Observatory and the Academia Sinica Institute of Astronomy and Astrophysics, and is funded by the Smithsonian Institution and the Academia Sinica.

3. RESULTS

3.1. CO (3–2) *Emission*

Figure 1 shows channel maps of the blueshifted and redshifted CO (3–2) emissions associated with I20126. For display purposes, we have smoothed the channel maps to a velocity resolution of 4.0 km s^{-1}. The outflow in CO (3–2) is detected to velocities $v_{\rm flow} \approx 51$ km s^{-1} in the redshifted lobe and $v_{\rm flow} \approx 57$ km s^{-1} in the blueshifted lobe, where $v_{\rm flow} \equiv |V_{\rm flow} - V_{\rm lsr}|$, with $V_{\rm flow}$ the apparent flow velocity and $V_{\rm lsr}$ (=−3.5 km s^{-1}) the systemic velocity of the source. In this paper we use the notation V for the apparent velocity and v for the velocity relative to the systemic velocity. Due to the lack of zero-spacing data to recover the extended emission filtered out by the interferometric observations, the CO (3–2) emission near the systemic velocity of the ambient cloud ($V_{\rm lsr} \pm$ 10 km s^{-1}) is not shown in Figure 1. The CO (3–2) emission integrated over the entire line wing (i.e., 11.0 km s$^{-1} \lesssim v_{\rm flow} \lesssim$ 57.0/51.0 km s^{-1} for the blueshifted/redshifted lobes) is shown in Figure 2. The position-velocity (P-V) diagrams of the CO (3–2) emission along P.A. of 120° and 150° are shown in Figure 3.

Three different components of outflowing gas can be identified in CO (3–2) emission:

1. First, as shown in Figure 2, the integrated CO (3–2) emission clearly describes the collimated outflow previously detected in SiO (2–1) (Cesaroni et al. 1997), with blueshifted gas located to the northwest and redshifted to the southeast. The P-V diagram of CO (3–2) along the axis of collimated SiO outflow (i.e., P.A. of

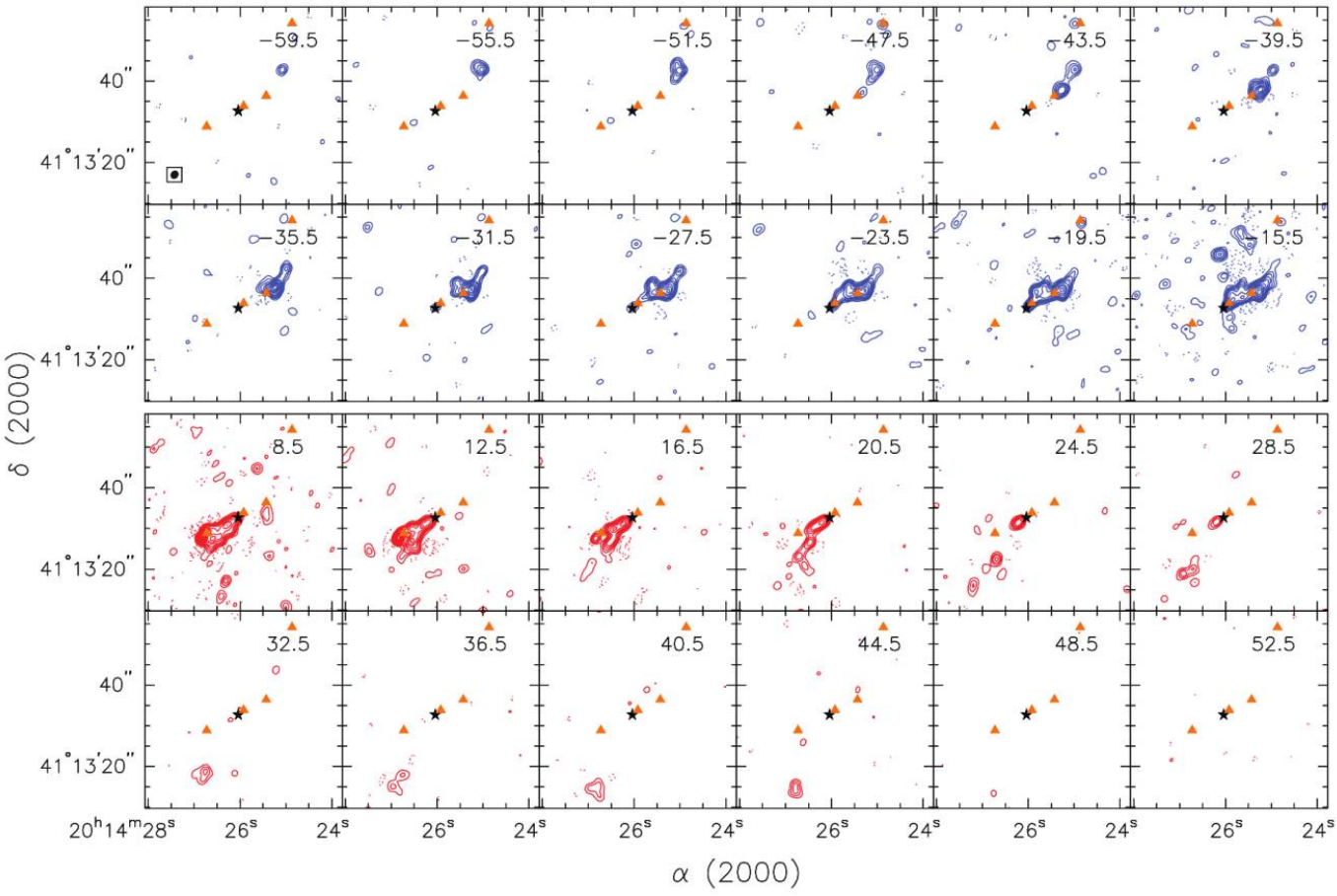

FIG. 1.—Channel maps of IRAS 20126+4104 in CO (3–2). The local standard of rest (LSR) velocity of each channel is indicated in the upper right corner of each panel. The LSR velocity of the system is -3.5 km s^{-1}. Solid contours are at 3, 7, 12, 20, 30, 50, 70, 90, 110, 130, 150, 170, and 190 $\times\,\sigma$, and dotted contours indicate -3, -7, -12, and $-20 \times \sigma$, where $\sigma = 0.05$ Jy beam^{-1}. The synthesized beam is shown in the lower left corner of the first panel. The star represents the centroid of 1.3 mm continuum from Cesaroni et al. (1999), and the triangles mark the positions of the H_2 knots from Shepherd et al. (2000).

$\sim$120°) shown in Figure 3 (*left*) further indicates that the velocity structures of the CO (3–2) and SiO (2–1) outflows are very similar. A discussion of the nature of this collimated outflow is presented in § 4.1.

2. Second, there is an S-shaped component with an extent of approximately 45″ (corresponding to $\sim$0.4 pc) along a P.A. of $\sim$150° with velocities $v_{\rm flow}$ up to $\approx$55 km s^{-1}. Similar to that seen in the collimated component, the blueshifted gas of the S-shaped component is located to the northwest and the redshifted gas to the southeast. Note that some blueshifted gas (from -55 to -15 km s^{-1}) of the S-shaped component is associated with a shock-excited H_2 knot which was denoted as H_2-1 by Shepherd et al. (2000). Since the H_2-1 knot is located beyond the primary beam of our SMA observations, its observed CO emission is significantly underestimated. The high-velocity ($v_{\rm flow} \gtrsim 20$ km s^{-1}) redshifted CO (3–2) gas, on the other hand, does not coincide with any known H_2 knot. The P-V diagram along the P.A. of 150° shown in Figure 3 (*right*) exhibits a distinctive kinematic feature, where the outflow velocity increases with distance from the central YSO presumably traced by the centroid of the 1.3 mm dust continuum. This is especially clear for the redshifted component. We discuss the nature of this component in § 4.2.

3. Finally, we identify a compact component with gas velocities $v_{\rm flow} \approx 20$–30 km s^{-1} in proximity to the central YSO, as shown in Figure 4. The projected separation between the high-velocity CO gas and the YSO is smaller than $\sim$2.5″ (corresponding to $\sim$4000 AU). This component demonstrates a bipolar structure along a P.A. of $\sim$120°, with blueshifted gas present to the northwest and redshifted gas to the southeast. The nature of this compact high-velocity outflow is described in § 4.3.

3.2. HCN (4–3) *Emission*

Figure 5 (*left*) shows the integrated emission of HCN (4–3) detected toward I20126. The HCN emission is concentrated along the axis of SiO (2–1) jet at the two outflow lobes and the central YSO. The two outflow lobes seen in HCN (4–3) correspond to the collimated CO (3–2) component. Toward the YSO, the HCN (4–3) emission arises from not only the dense core but also the CO (3–2) compact bipolar outflow. No HCN (4–3) emission is detected toward the S-shaped component seen in CO (3–2). The two HCN (4–3) outflow lobes are marginally resolved with a synthesized beam of $\sim$1.6″ and have a comparable deconvolved angular size of approximately 2″, corresponding to a linear size of $\sim$3000 AU. The core component is even more compact, with a deconvolved angular size of only 1.3″.

The P-V diagram of the HCN (4–3) emission along the P.A. of 120° is shown in Figure 6 (*left*). The velocity dispersion is $\sim$35 km s^{-1} in the southeast lobe and $\sim$55 km s^{-1} in the northwest lobe. There is no obvious dependence of velocity on position within each lobe. By comparing the P-V diagrams (Fig. 3, *left*, and Fig. 6, *left*), we find similar velocity extents for both CO (3–2) and HCN (4–3) at the three locations. The apparent difference seen in

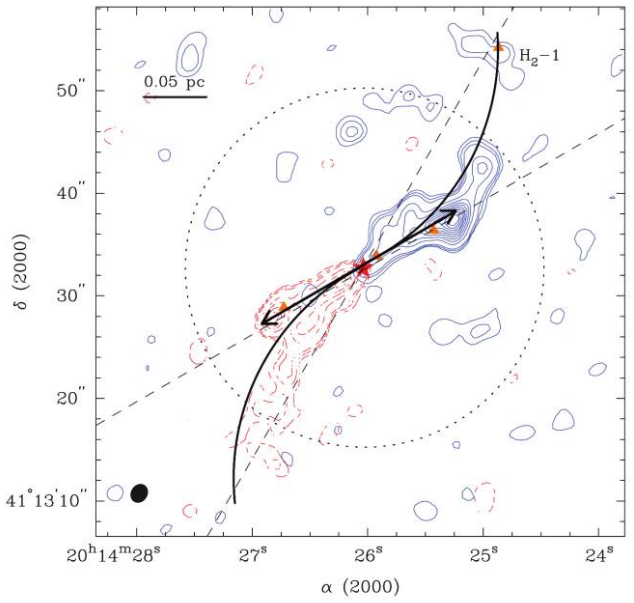

FIG. 2.—Bipolar molecular outflow of IRAS 20126+4104 in CO (3–2) integrated over the entire line wing (11.0 km s^{-1} $\lesssim v_{\rm flow} \lesssim$ 57.0/51.0 km s^{-1} for the blueshifted/redshifted lobes). Blueshifted and redshifted emissions are shown by solid and dashed contours, respectively. Contours are 2.1, 4.2, and from 7.0 to 133 in steps of 14.0 Jy beam^{-1} km s^{-1}. The two dashed lines represent the axes of the position-velocity diagrams in Fig. 3, and the dotted circle represents the primary beam of the SMA observations. The synthesized beam is shown in the lower left corner. The star indicates the centroid of 1.3 mm continuum from Cesaroni et al. (1999), and the triangles mark the positions of the H_2 knots from Shepherd et al. (2000). The collimated outflow and the S-shaped outflow are labeled by thick lines.

the redshifted gas toward the YSO is likely due to the blending of the HCN ($\nu_2 = 1$, 4–3) transition (as shown in Fig. 7), which is responsible for the detection of the HCN emission up to $V_{\rm flow} \simeq +50$ km s^{-1} in comparison with the maximum velocity $V_{\rm flow} \approx +30$ km s^{-1} of the detectable CO (3–2) emission. The vibrationally excited HCN ($\nu_2 = 1$, 4–3) transition appears only in the core component, and the nondetection toward the outflow lobes is unlikely due to the sensitivity effect for the following reason. Assuming a similar ratio of the HCN (4–3) intensity to the HCN ($\nu_2 = 1$, 4–3) intensity, we expect a detection at $\sim$15 σ level for this vibrationally excited HCN transition toward the outflow lobes. We discuss the nature of this vibrationally excited transition in § 4.4.3.

Using the line ratios among isotopomers, we can estimate the optical depth of the observed HCN (4–3) emission. Our SMA observations also detect HC^{15}N (4–3) toward the YSO with a peak intensity approximately 2 times smaller than that of HCN (4–3) (S.-Y. Liu et al. 2008, in preparation). Assuming the same excitation temperature and beam filling factor for HCN and HC^{15}N, the optical depth of the HCN emission can be roughly estimated from the equation

$$\frac{S_\nu[\mathrm{HCN}(4\text{–}3)]}{S_\nu\left[\mathrm{HC^{15}N}(4\text{–}3)\right]} \simeq \left(\frac{1-e^{-\tau}}{1-e^{-\tau_1}}\right), \qquad (1)$$

where τ and τ_1 are the opacities of HCN (4–3) and HC^{15}N (4–3), respectively, and $\tau/\tau_1 = [^{14}\mathrm{N}]/[^{15}\mathrm{N}]$. Given the distance to Galactic center of approximately 7 kpc for I20126, an abundance ratio $[^{14}\mathrm{N}]/[^{15}\mathrm{N}] \approx 400$ is inferred from Wilson & Rood (1994). Such an abundance ratio indicates that toward the central YSO the HCN (4–3) emission is optically thick, with an opacity $\approx$300, and toward the outflow lobes the nondetection of the HC^{15}N emission leads to an HCN (4–3) opacity upper limit of $\sim$15.

3.3. SiO (5–4) *Emission*

Figure 5 (*right*) shows the integrated SiO (5–4) emission overlaid on the integrated HCN (4–3) detected toward I20126. The SiO (5–4) emission is mainly concentrated in the two outflow lobes and demonstrates a bowlike structure in both lobes, while weak SiO emission is also identified toward the central YSO (from -8 to -2 km s^{-1}; see Fig. 6, *right*) and the near-IR H_2-1 knot (from -16 to -12 km^{-1}; see Fig. 8). Both SiO (5–4) lobes are very compact and have a similar projected linear size of 2000–4000 AU. The compact bipolar outflow seen in CO (3–2) and HCN (4–3) is not detected in SiO (5–4), likely due to a sensitivity effect. The S-shaped component detected in CO (3–2) is also not seen in SiO (5–4). The SiO (5–4) outflow lobes coincide spatially with the HCN (4–3) clumps and near-IR H_2 spots roughly, although a spatial differentiation between HCN (4–3) and SiO (5–4), especially in the southeast lobe, can be discerned. Figure 6 (*right*) displays the P-V diagram of the SiO (5–4) line along a P.A. of 120°. The SiO (5–4) emission is clearly detected from -18 to +14 km s^{-1}, and there appears to have high-velocity blueshifted gas from -40 to -20 km s^{-1} (corresponding to $v_{\rm flow} \approx$ 17–37 km s^{-1}). The velocity structure of the SiO (5–4) emission along the jet axis is very similar to that of HCN (4–3). The velocity dispersion is $\sim$35 km s^{-1} in the southeast lobe and $\sim$45 km s^{-1} in the northwest lobe. No clear velocity dependence on position within each SiO lobe can be detected.

The velocity extent of the SiO (5–4) line is not as broad as that of the SiO (2–1) transition, which can be detected from -50 to +25 km s^{-1} (Cesaroni et al. 1999). Furthermore, the integrated SiO (5–4) emission demonstrates a bow-shaped structure, while the integrated SiO (2–1) emission exhibits a clear jet-like morphology (i.e., a small-opening angle outflow with an extension from the YSO to the bow [jet] tips). Assuming the same physical conditions of the SiO gas at different velocities, the line wings revealed in the SiO (2–1) transition appear to be too weak to be detected by our SiO (5–4) observations. Therefore, the difference in velocity extent likely results from varied brightness temperature sensitivities in observations. The distinction in morphology of the SiO (2–1) and (5–4) emissions, however, is unlikely to be caused by the sensitivity and/or *u-v* coverage issues. Assuming a similar line ratio of SiO (5–4)/SiO (2–1) measured toward the two lobes, we expect to detect a jet-like morphology in SiO (5–4) at approximately 5 σ levels. Also, the shortest baselines of the SiO (2–1) and (5–4) observations are very similar, about 12 and 16 kλ, respectively. The corresponding largest detectable structure is $\sim$6″–7″, approximately twice as large as the detected emission scales. Therefore, we conclude that the excitation toward the two lobes is higher than other regions seen in SiO (2–1).

4. DISCUSSION

Using our new SMA measurements, we now discuss possible scenarios of the outflow/jet using a variety of tracers over scales ranging from a few thousand AU to $\sim$0.4 pc. In particular, we examine the precession history using the kinematic structure observed in the S-shaped CO (3–2) outflow, and derive the physical conditions in I20126 shocks using the large velocity gradient calculations.

4.1. *The Jet-driven Bow Shock System*

The details of outflow-driving mechanisms are still not clear, although outflows have been identified as a common phenomenon of star formation. The observed outflow characteristics usually favor the jet-driven bow shock models and wind-driven-shell models (for a recent review, see Arce et al. 2007). In the jet-driven bow

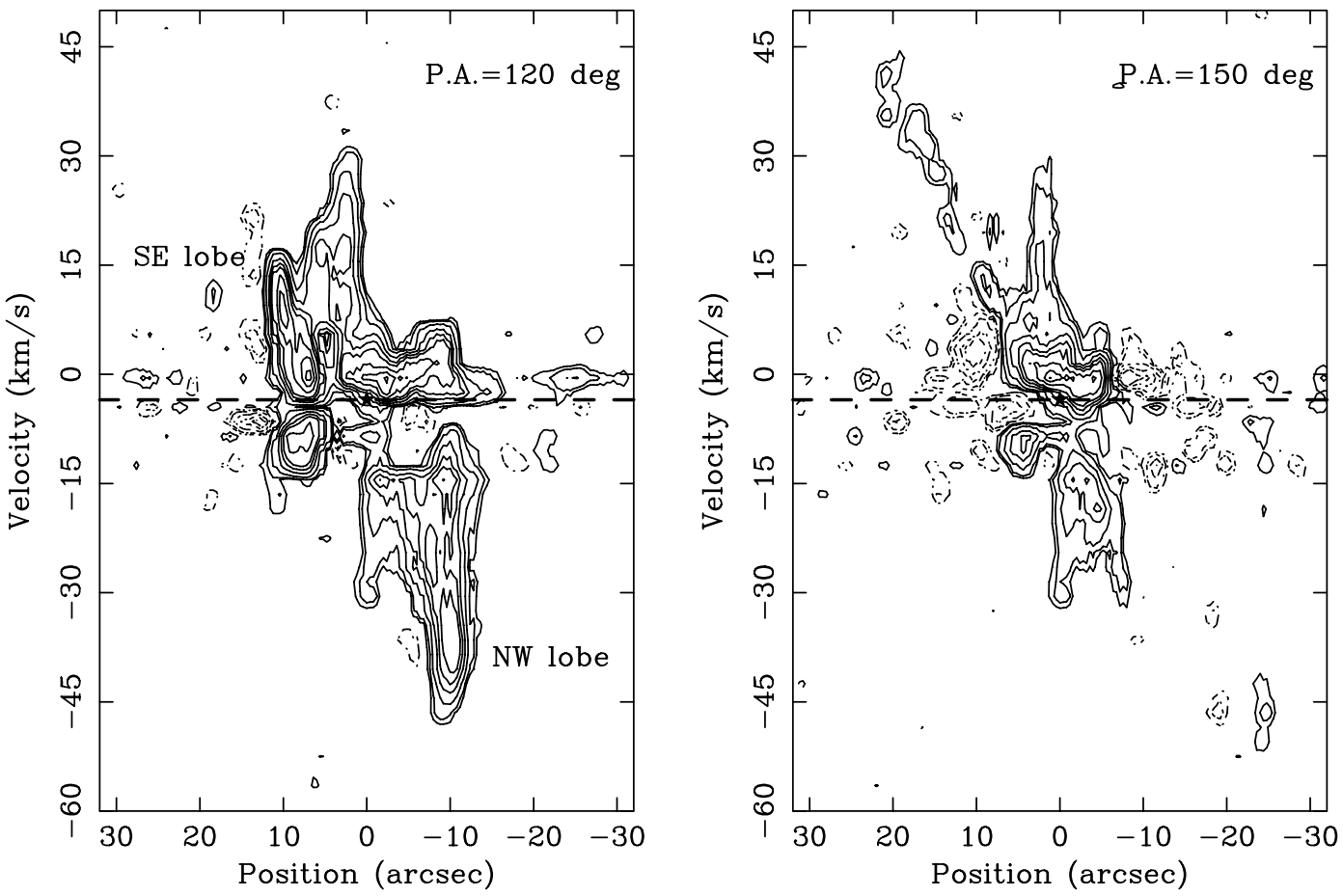

FIG. 3.—Position-velocity diagram of IRAS 20126+4104 CO (3–2) outflow along a P.A. of 120° (*left*) and 150° (*right*). In each panel, the dashed horizontal line marks the LSR velocity of the system (i.e., −3.5 km s^{-1}), and the star indicates the position of the 1.3 mm continuum from Cesaroni et al. (1999).

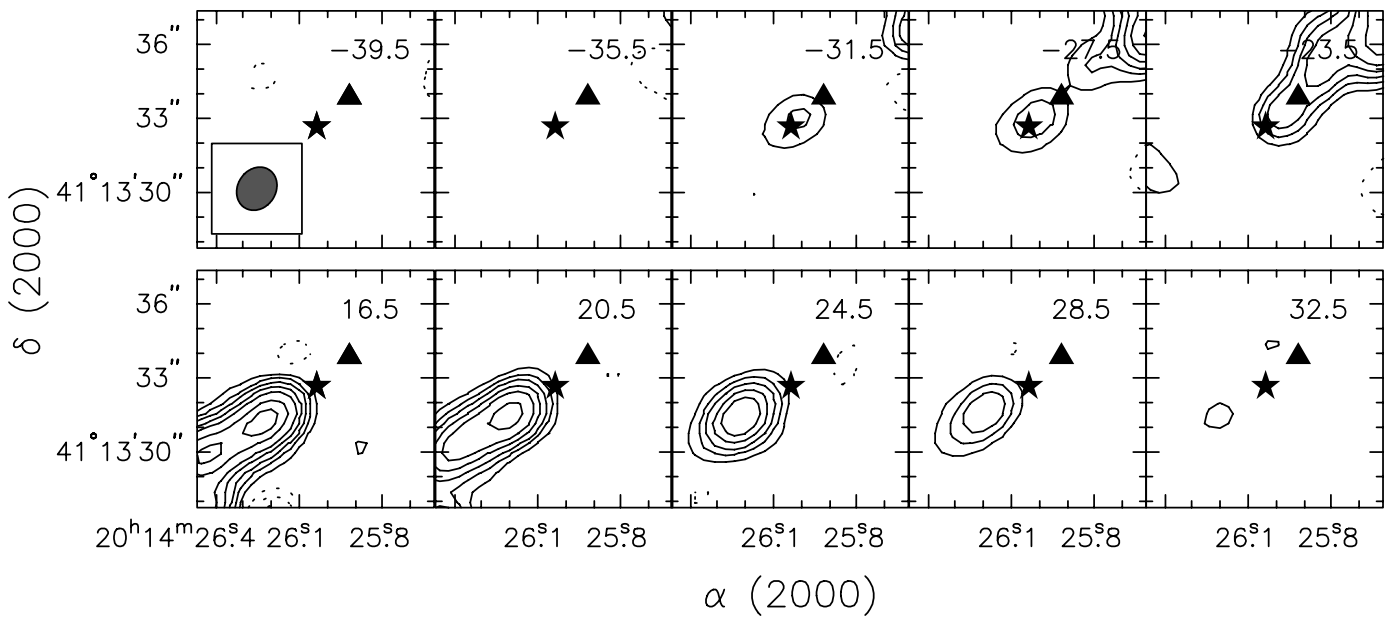

FIG. 4.—Same as in Fig. 1, but zooming in the central region for blueshifted channels from −39.5 to −23.5 km s^{-1} and redshifted channels from 16.5 to 32.5 km s^{-1}. The LSR velocity of the system is −3.5 km s^{-1}.

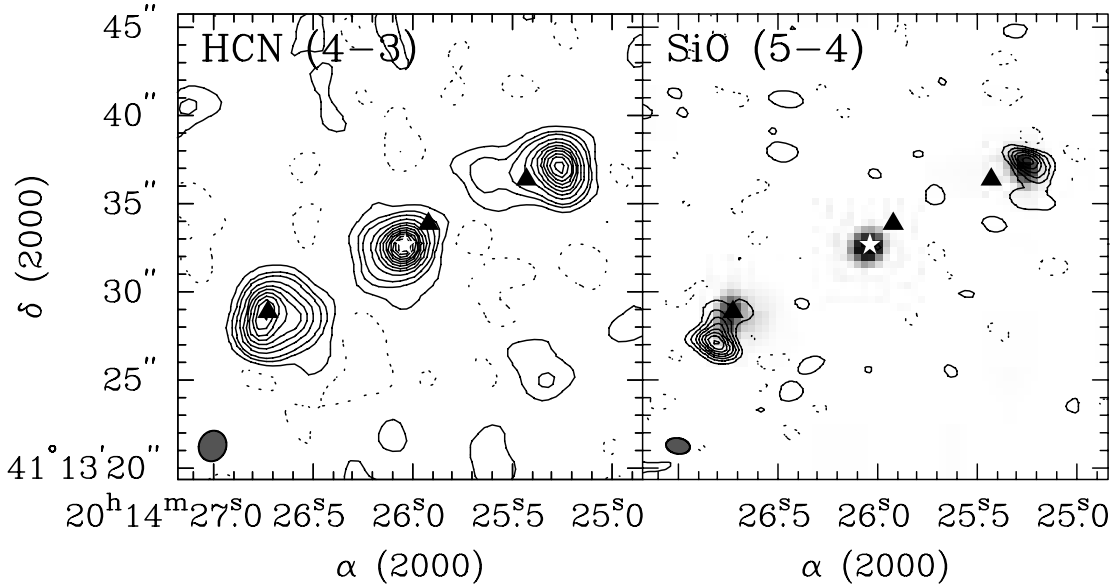

FIG. 5.—Contour plots of the integrated HCN (4–3) (*left*) and SiO (5–4) (*right*) emission. The HCN (4–3) line is integrated from −48 to 24 km s^{-1}, and the SiO (5–4) from −40 to 16 km s^{-1}. The LSR velocity of the system is −3.5 km s^{-1}. In the right panel, the gray scales represent the integrated HCN (4–3) emission. Contour levels are −6.4, −2.4, 2.4, 6.4, and from 10.4 to 90.4 in steps of 8.0 Jy beam^{-1} km s^{-1} in the left panel, and −0.9 and from 0.9 to 7.2 in steps of 0.9 Jy beam^{-1} km s^{-1} in the right panel. The dark ellipse in each panel denotes the synthesized beam. The star indicates the centroid of 1.3 mm continuum from Cesaroni et al. (1999), and the triangles mark the positions of the H_2 knots from Shepherd et al. (2000).

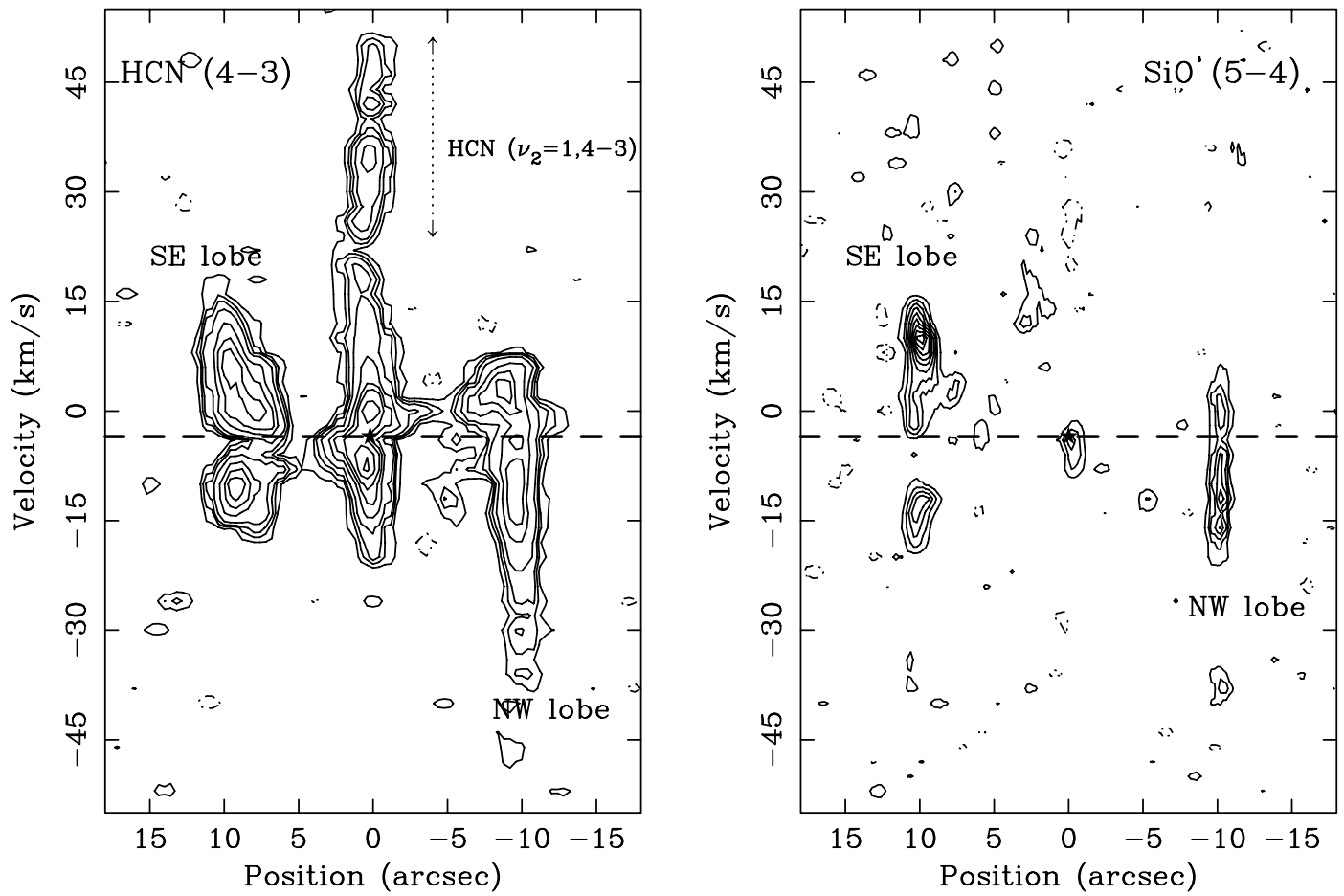

FIG. 6.—Position-velocity diagram of the HCN (4–3) (*left*) and SiO (5–4) (*right*) lines along the collimated outflow axis (i.e., P.A. = 120°). In the left panel, the emission which likely arises from HCN ($\nu_2 = 1, 4–3$) is labeled. In each panel, the dashed horizontal line marks the LSR velocity of the system (i.e., −3.5 km s^{-1}), and the star indicates the position of the 1.3 mm continuum from Cesaroni et al. (1999).

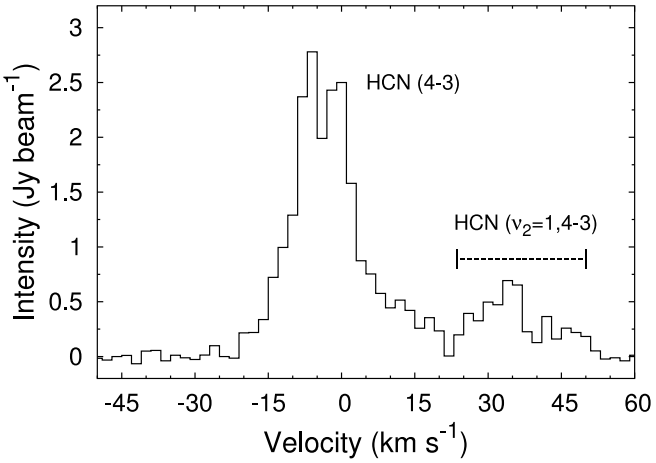

FIG. 7.—Spectrum of HCN (4–3) toward the YSO in I20126. The emission which likely arises from HCN ($\nu_2 = 1$, 4–3) is labeled.

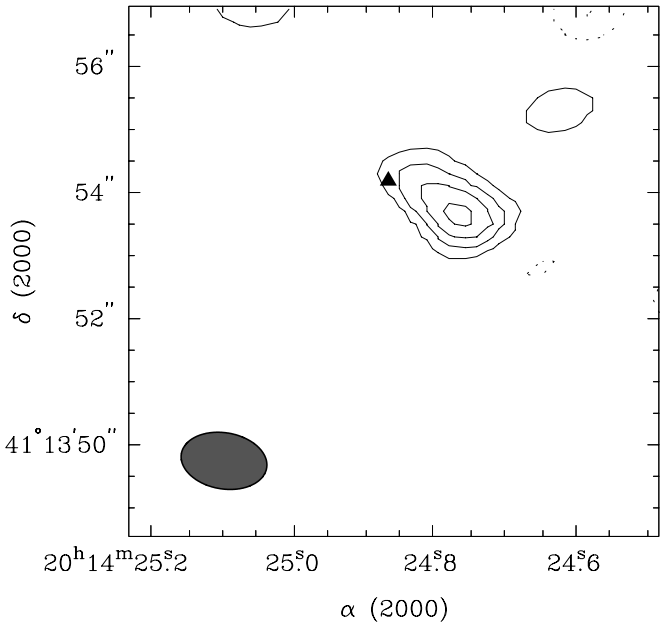

FIG. 8.—Contour plots of the SiO (5–4) emission toward the H_2-1 knot. The SiO (5–4) line is integrated from −16 to −12 km s^{-1}. Contour levels are −0.27, 0.27, 0.45, 0.63, and 0.81 Jy beam^{-1} km s^{-1}. The dark ellipse in the bottom left denotes the synthesized beam, and the triangle marks the position of the H_2-1 knot from Shepherd et al. (2000).

shock model, a bow shock forming at the head of the jet interacts with the ambient gas and produces a molecular outflow (Raga & Cabrit 1993). In the wind-driven shell model, a wide-angle wind expelled from a young star blows into the surrounding ambient gas, producing a molecular outflow (Shu et al. 1991). The primary jet (wind) is responsible for furnishing sufficient energy and momentum to drive the molecular outflow. Observationally, in several outflows two distinguishable components can be discerned—a "classical" component, which appears less collimated and of low velocity, and a collimated, high-velocity component. One of the best examples is HH 211, where the low-velocity gas describes a pair of cavities and the high-velocity component exhibits a well-collimated jetlike structure (Gueth & Guilloteau 1999). The jet is associated with a chain of SiO knots, and the innermost knots are suggested to trace the primary jet launched close to the protostar (Hirano et al. 2006; Palau et al. 2006).

In the case of I20126, a small-scale outflow with an extent of ∼20″ (corresponding to ∼0.2 pc) have been identified in several tracers such as SiO (2–1), HCO^+ (2–1) and near-IR H_2 emissions (Cesaroni et al. 1997, 1999; Shepherd et al. 2000). The SiO (2–1) emission shows a jetlike structure, while the outflow in HCO^+ appears more "classical." Cesaroni et al. (1999) proposed a possible scenario that the less-collimated low-velocity HCO^+ outflow is fed by the collimated SiO jet. From our SMA observations, CO (3–2) also describes the jetlike morphology seen in SiO (2–1), while the emissions of SiO (5–4) and HCN (4–3), both recognized as good tracers of shocks, are concentrated only in the jet tips associated with the near-IR shock-excited H_2 knots. In particular, the integrated SiO (5–4) emission exhibits a bow-shaped structure. The morphology of the collimated outflow thus favors the jet-driven bow shock models.

Kinematically speaking, as shown in Figure 6, both the HCN (4–3) and SiO (5–4) emissions exhibit a similar structure—the gas at the outflow lobes shows a broad range of velocities (∼35–55 km s^{-1}). Similar features have been revealed in outflows from other star formation regions (e.g., Sollins et al. 2004 and references therein). Such broad line widths at the head of the jet are consistent with the prediction of jet-driven bow shock models (e.g., Lee et al. 2001). On the contrary, wind-driven models exhibit only a small velocity range at the outflow tip. Therefore, the evidence in both morphology and kinematics suggests that the observed collimated SiO (5–4), HCN (4–3), and CO (3–2) gas describes a jet-driven bow shock system.

4.2. *The* S*-shaped* CO *Emission and the Jet Precession*

The integrated CO (3–2) emission clearly comprises an S-shaped structure and appears to trace the near-IR H_2 knots well. One likely interpretation for this morphology is that the S-shaped CO (3–2) gas has a close relation to the precessing jet. As mentioned in § 1, the S-shaped distribution of the H_2/Hα knots has been argued as resulting from the precession of the primary jet and likely marks the precession history (e.g., Shepherd et al. 2000; Cesaroni et al. 2005). Moreover, the gradual change of outflow axis from small (∼20″) to large (∼2′) scales provides another piece of evidence for the precession (Cesaroni et al. 1999; Lebrón et al. 2006; Shepherd et al. 2000).

Assuming a constant outflow velocity and that the H_2 and Hα knots trace the working surface of a precessing jet, a precession history was derived by fitting the kinematic structure of the SiO jet and the distributions of the H_2 and Hα knots (e.g., Cesaroni et al. 1999, 2005). The authors concluded the following: (1) The collimated SiO jet is aligned very close (∼9°) to the plane of the sky. (2) Due to precession, the northwest part (i.e., the blue lobe) of the outflow is moving away from the observer, while the southeast part (i.e., the red lobe) of the outflow is approaching us. In addition to morphologies, one can further examine the *kinematic structure* of the jet/outflow to test the hypothesis of precession. For example, the kinematics of water maser spots suggest that on scales of a few hundred AU the jet has already crossed the plane of the sky (Moscadelli et al. 2005), consistent with the precessing direction proposed by Cesaroni et al. (2005).

An examination of large-scale kinematics, however, was not possible because of the missing velocity information of the H_2 imaging. In contrast, if the S-shaped CO (3–2) gas has a close relation to the primary jet, its velocity structure should play an essential and independent role in probing the precession history. As shown in Figure 3 (*right*), the velocity (along the line of sight) of the redshifted S-shaped gas increases with distance from the central YSO.

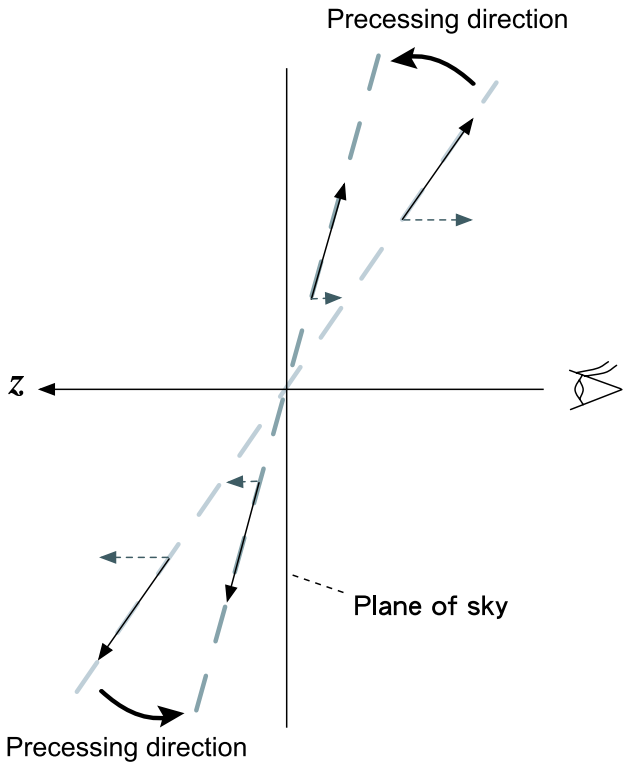

FIG. 9.—Schematic view of the kinematics structure of the precessing outflow in I20126. Each of the two dashed lines indicates the direction of the primary jet. Because the present outflow axis is almost aligned on the plane of the sky and both the red and blue lobes are approaching the plane of the sky (Cesaroni et al. 1999, 2005), the light gray is earlier in time than the dark gray. The figure demonstrates that the projected velocity (onto the line of sight) of the CO (3–2) gas will increase as its distance to the outflow centroid due to the change of the inclination (i.e., from the plane of the sky to the line of sight). This velocity structure is qualitatively consistent with the kinematic structure observed in the S-shaped CO (3–2) outflow.

The assumption of the primary jet having a constant velocity with time (Cesaroni et al. 2005) would infer a constant velocity of the CO (3–2) outflowing gas. In this case, the distinctive velocity gradient seen in Figure 3 (*right*) should be the result of a projection effect, and the observed downstream CO (3–2) gas was ejected earlier and hence propagates further from the driving young star.

The observed kinematic feature indicates that both the red and blue lobes are approaching the plane of the sky and the radial velocity will increase with distance to the outflow centroid because of the decrease in inclination (i.e., from the plane of the sky to the line of sight). A schematic view of this picture is shown in Figure 9. We note that although the above arguments are mainly based on the velocity structure seen in the redshifted gas, the kinematics of the blueshifted gas also support the hypothesis of precession. As shown in Figure 3 (*right*), the blueshifted CO gas at the H_2-1 knot is perfectly symmetric in position and velocity with respect to the redshifted component. Thus, we conclude that the S-shaped CO (3–2) emission records the precession history very well, at least on scales of $\sim$0.4 pc, and its kinematic structure suggests that, due to the precession, the outflow axis is moving toward the plane of the sky. The precessing direction inferred here from the kinematics of CO (3–2) gas is consistent with that deduced from the outflow morphology by Cesaroni et al. (1999, 2005). The present kinematics of the S-shaped gas allow us to further clarify the relationship between the S-shaped CO gas and H_2 emission if the kinematics of the H_2 knots are available.

In addition to the case of I20126, precessing outflows are not very unusual, and have been detected at (sub)millimeter, near-IR, and optical wavelengths toward both low-mass and high-mass YSOs, for example, L1157 (Gueth et al. 1996; Bachiller et al. 2001), Cep E (Eislöffel et al. 1996), HH 333 (Bally et al. 1996), and NGC 7538 IRS1 (Kraus et al. 2006). In most low-mass cases, the precession angle (i.e., the opening angle of the precession cone) is less than 10°. Two possible mechanisms leading to such a jet precession have been proposed by Fendt & Zinnecker (1998), including the motion of the jet driving the source in a coplanar-orbital binary system (i.e., the jet axis being perpendicular to the plane of the binary orbit) and the action of Lorentz forces between (ionized) jet and interstellar magnetic field. However, neither can create the large precession angle of $\gtrsim 40^\circ$ seen in I20126 and NGC 7538 IRS1. Shepherd et al. (2000) discussed several possible mechanisms which can cause large precession angles and favored the presence of a companion in a noncoplanar orbit for I20126. Kraus et al. (2006) also preferred the same interpretation for the large precession angle discovered in NGC 7538 IRS1. Identifications of the companion and measurements of the orbital parameters are essential to confirm whether the precession is actually caused by the presence of a companion.

4.3. *The Nature of the Compact Outflow*

As mentioned in § 3, we detected compact high-velocity (20–30 km s^{-1}) gas in CO (3–2) and HCN (4–3) toward the central YSO. This component clearly demonstrates a bipolar structure and is very close to the YSO, with a projected distance smaller than $\sim$4000 AU (see Fig. 4). Assuming an inclination angle (with respect to the line of sight) of $\sim 80^\circ$, the dynamical timescale of this component is approximately 120 yr only. In this case, the deprojected outflow velocity is about 170 km s^{-1}, among the highest velocities that have been observed in molecular outflowing gas.

The bulk of the molecular outflow detected in low-J CO lines is thought to mainly comprise swept-up ambient molecular gas entrained by a high-velocity wind/jet from the central young star (Bachiller & Tafalla 1999). The mechanisms of entrainment are not well understood, and the composition of the primary jet/wind which is responsible for accelerating the ambient material has not been identified. Molecular outflows often show a power-law relation between mass and velocity, i.e., $m(v) \propto v^{-\gamma}$, with a typical power index γ around 1.8. In many cases, however, the mass spectrum has a broken power law, with the slope steepening at high velocity ($v_{\rm flow} \gtrsim 10$ km s^{-1}; Richer et al. 2000; Su et al. 2004). One possible explanation for the distinct behavior between high- and low-velocity gas is that the high-velocity molecular gas is closely connected to the primary jet (Bachiller & Tafalla 1999).

To examine this hypothesis in I20126, we estimate whether the momentum supply rate of this compact component is sufficient to drive the molecular outflow seen in CO (1–0). As shown in Figure 4, it is difficult to separate the compact component from other outflowing gas. Here we calculate the momentum supply rate using only the high-velocity redshift gas with velocity $V_{\rm flow}$ between 24.5 and 32.5 km s^{-1}, where the contamination is much less severe. Assuming a gas temperature of $\sim$100 K, an inclination angle of $\sim 80^\circ$, and that the CO (3–2) wing emission is optically thin, following Su et al. (2004) the inferred momentum supply rate is approximately $1 \times 10^{-3}\, M_\odot$ km s^{-1} yr^{-1}. Although this is a factor of 6 smaller than that derived from CO (1–0) observations by Shepherd et al. (2000), it is still possible that the thrust of the compact component is sufficient to drive the CO (1–0) outflow due to the following two reasons. First, because there is significant contamination from other components, the contributions of the blueshifted component and the "low-velocity" redshifted part are not included in our estimation. Second, observations of water maser emission suggested that on scales of a few hundred

AU the jet has already crossed the plane of the sky (Moscadelli et al. 2005). Thus, the compact component may be even closer to the plane of the sky, causing the thrust to be underestimated here. We note that the momentum supply rates of the small-scale collimated SiO jet and the large-scale CO (1–0) outflow appear to be comparable. The momentum supply rate inferred from the SiO (2–1) jet scaling to an SiO abundance of $(1–5) \times 10^{-8}$ (see § 4.4.1) and correcting for the inclination is approximately (6×10^{-3})–(3×10^{-2}) $M_\odot$ km s^{-1} yr^{-1} (Cesaroni et al. 1999). On the other hand, the discontinuity of the near-IR H_2 emission suggests episodic activities in I20126 outflow. If this is the case, the pulses of the momentum supply rate derived from the episodic (primary) jet should be large than that from the "classical" outflow due to the short timescale of the episodic activities. A detailed study of the time interval of the episodic events is required to conclude whether the thrust of the compact CO (3–2) gas is sufficient to drive the large-scale outflow seen in CO (1–0). Alternatively, two other possible compositions (i.e., atomic gas and ionized gas) of the primary jet should be considered if the thrust of the high-velocity molecular gas is actually not sufficient.

In summary, all the three outflow components seen in CO (3–2) have a close relation to the primary jet undergoing precession over scales ranging from ~4000 AU to ~0.4 pc. With extremely high velocity (~170 km s^{-1}) gas and a very short dynamical timescale (~120 yr), the innermost compact (~4000 AU) component represents a very latest outflowing event. Both the morphology and kinematics suggest that the collimated component with an extent of ~0.2 pc describes a jet-driven bow shock currently interacting with the ambient gas. Finally, on scales of ~0.4 pc, the S-shaped CO gas records the history of the (primary) jet precession very well. Its kinematics suggest that, due to precession, the outflow axis is moving toward the plane of the sky. The morphologies of the three components further suggest episodic activities in the I20126 outflow. We note that the redshifted gas of the compact component is not detected in the CO (1–0) emission reported by Shepherd et al. (2000). We conclude that high-velocity ($v_{\rm flow} \gtrsim 10$ km s^{-1}) CO (3–2) emission is a good tracer to probe the primary jet.

4.4. *Shocks and High-Excitation Regions in IRAS 20126+4104*

SiO and HCN have been recognized as good tracers of shocks. Both theoretical models and observational results suggest that SiO abundances can be enhanced by several orders of magnitude at the head and along the axes of molecular outflows (e.g., Schilke et al. 1997; Bachiller 1996 and references therein). The abundance of HCN in a chemically active outflow lobe of L1157 is enhanced by 2 orders of magnitude with respect to the prestellar core (Bachiller & Pérez Gutiérrez 1997).

In the case of I20126, the strong SiO (5–4) and HCN (4–3) emissions are closely related to the shock-excited near-IR H_2 knots. A spatial differentiation between SiO (5–4) and HCN (4–3), however, can be discerned in the I20126 outflow, as shown in Figure 5. The SiO (5–4) emission mainly arises from the bow tips, while the HCN (4–3) emission is associated with the shock wings. This is especially clear in the southeast lobe. A similar spatial differentiation between CH_3OH and SiO (2–1) toward I20126 outflow had been reported by Cesaroni et al. (2005). In addition, there appears to be a similar spatial segregation between SiO and HCN in the outflow from the low-mass YSO L1157 (Bachiller et al. 2001). The spatial differentiation may result from different physical conditions and chemical reaction networks in shocked regions.

4.4.1. *Physical Conditions Inferred from* SiO *Lines*

We explore the physical conditions of the shocked regions with large velocity gradient (LVG) calculations using our SMA SiO (5–4) data and the SiO (2–1) results reported by Cesaroni et al. (1999). We used the LVG code written by L. G. Mundy and implemented as part of the MIRIAD package (Sault et al. 1995). In order to compute the line ratio of the two SiO transitions, we convolved the SiO (5–4) channel maps to a Gaussian beam of $1.8'' \times 1.6''$ to match the angular resolution of the SiO (2–1) maps. The SiO (5–4)/(2–1) line ratios are in the range 1–2. Assuming a gas temperature of ~300 K, similar to that in the low-mass cases (e.g., Nisini et al. 2007), the LVG calculations suggest at both lobes gas densities of $(2–4) \times 10^5$ cm^{-3} and SiO relative abundances X(SiO) of $(1–5) \times 10^{-8}$. The inferred SiO abundance and gas density will be approximately an order of magnitude lower and higher, respectively, if a gas temperature as low as 30 K is assumed. The inferred SiO abundances in the I20126 outflow lobes are consistent with the picture of enhancement in shocked regions, as identified at low-mass outflows. Recently, a study of multiple SiO transitions suggested an SiO abundance of a few $\times 10^{-8}$ in L1448 and L1157 bullets (Nisini et al. 2007), while in typical dark clouds the X(SiO) is less than 10^{-11} (Ziurys et al. 1989).

4.4.2. *Physical Conditions Inferred from* HCN (4–3)

With its high critical densities $\gtrsim 10^6$ cm^{-3}, HCN is often used to trace dense molecular gas. Indeed, HCN transitions have been detected toward Class 0 and Class I low-mass YSOs and in hot molecular cores associated with high-mass YSOs (e.g., Park et al. 1999; Hatchell et al. 1998). From a chemistry viewpoint, HCN plays an essential role in nitrogen chemistry in hot-core sources and shocked regions (Viti & Williams 1999a, 1999b). The abundances of HCN in molecular outflows can be enhanced by 2 orders of magnitude with respect to their core components (e.g., Bachiller & Pérez Gutiérrez 1997). The enhancement is attributed to shock chemistry.

We assume the HCN (4–3) emission to be optically thin and in LTE with a gas temperature of 300 K, and derive an HCN column density of $(1–2) \times 10^{14}$ cm^{-2} in I20126 outflow lobes. Due to the lack of a direct estimate of the gas column density toward HCN outflow lobes, we assume a gas column density of $\sim 1 \times 10^{22}$ cm^{-2} inferred from SiO emission, although a spatial variation in density may occur. We estimate an HCN abundance of $\sim(1–2) \times 10^{-8}$ in the outflow lobes. The assumption of optically thin emission results in an underestimation of the column density and hence the abundance of HCN if the HCN (4–3) emission is actually optically thick toward the outflow lobes. The inferred HCN abundance is about an order of magnitude larger than that seen in outflows and star-forming cores (Jørgensen et al. 2004), but approximately an order of magnitude smaller than that seen in the L1157 outflow (Bachiller & Pérez Gutiérrez 1997).

4.4.3. *The Nature of the Vibrationally Excited* HCN *Emission*

As mentioned in § 3.2, toward the YSO the vibrationally excited HCN ($\nu_2 = 1$, 4–3) is detected. With with an upper energy level of ~1000 K, this detection cannot be explained by collisional pumping of gas at ~25 K, corresponding to the peak brightness temperature of the optically thick HCN (4–3) emission. Below we discuss three possible origins of the HCN ($\nu_2 = 1$, 4–3) emission. First, since the core size inferred from the HCN ($\nu_2 = 1$, 4–3) emission is approximately a factor of 3 smaller than that from HCN (4–3), a temperature profile of $T \propto r^{-a}$, $a = 2$, can solve the problem. Another possibility is that the HCN gas has a small filling factor and hence the gas temperature is underestimated when assuming $T_b = T_{\rm gas}$. A filling factor of ~0.1 will be able to interpret the detection of HCN ($\nu_2 = 1$, 4–3). Finally, the vibrationally excited HCN line can also result from

infrared pumping due to the powerful infrared radiation fields generated by the surrounding warm, obscure dusty envelope. This further explains the nondetection of HCN ($\nu_2 = 1$, 4–3) toward the outflow lobes. We note that the HCN ($\nu_2 = 1$, 4–3) emission is also detected toward the massive star-forming core G9.62+0.19-F (Y.-N. Su et al. 2008, in preparation). G9.62+0.19-F likely harbors a high-mass protostar, and hence can emit strong infrared radiation fields.

5. SUMMARY

I20126 provides a unique laboratory for better understanding the properties of outflows from massive young stars. We have imaged the outflow associated with the luminous YSO I20126 in CO (3–2), HCN (4–3), and SiO (5–4) with the SMA at angular resolutions of 1″–2″. Our main results can be summarized as follows:

1. Observations in CO (3–2) reveal at least three different components of the outflowing gas: a compact high-velocity component toward the YSO (within a projected distance smaller than ∼4000 AU), a collimated bipolar outflow with an extent of ∼0.2 pc previously detected in SiO (2–1), and an S-shaped component with an extent of ∼0.4 pc symmetric with respect to the central young star.

2. Assuming an inclination of ∼80° (with respect to the line of sight) for the compact component, we obtain a deprojected velocity of ∼170 km s^{-1}, among the highest gas velocities that have been detected in molecular outflows. With a dynamical timescale ∼120 yr, the compact component represents a very latest outflowing event in I20126.

3. The collimated outflow is also detected in HCN (4–3) and SiO (5–4). The morphology and kinematic structure of the collimated component seen in CO, SiO, and HCN all favor a jet-driven bow shock system in I20126. Furthermore, a spatial differentiation between SiO (5–4) and HCN (4–3) can be discerned in the two outflow lobes. The former mainly arises from the bow tips and the latter from the shock wings. The spatial segregation may result from the different physical conditions and chemical reaction networks in shocked regions.

4. The S-shaped CO (3–2) emission appears to trace (on the scales of ∼0.4 pc) the near-IR H_2 knots, an indicator of precession in I20126 outflow. The S-shaped CO gas exhibits a dramatic kinematic feature, where the outflow velocity increases with distance from the YSO. The kinematic structure indicates, independently of other evidence, that the outflow axis is moving toward the plane of the sky due to precession. The inferred precessing direction is consistent with that proposed by Cesaroni et al. (1999, 2005) based on the outflow morphology. We conclude that the S-shaped CO (3–2) emission can trace well the precession history, at least on scales of ∼0.4 pc.

5. All the three outflow components seen in CO (3–2) are closely related to the precessing primary jet over scales ranging from a few thousand AU to ∼0.4 pc. The morphologies of the three components further suggest episodic activities in I20126 outflow. Our SMA results indicate that high-velocity ($v_{\rm flow} \gtrsim 10$ km s^{-1}) CO (3–2) emission is a good tracer to probe the primary jet.

6. The physical conditions of the shocked regions are inferred with the line ratio of SiO(5–4)/SiO(2–1). Assuming a gas temperature of 300 K, the LVG calculations suggested that at both lobes gas densities of $(2–4) \times 10^5$ cm^{-3} and SiO relative abundances X(SiO) of $(1–5) \times 10^{-8}$. The inferred SiO abundances in I20126 outflow lobes are comparable to the expected enhancement at shocked regions.

We acknowledge valuable comments from the anonymous referee. We thank all SMA staff for their help during these observations. S.-Y. L., Y.-N. S., and H.-R. C. thank the National Science Council of Taiwan for support this work through grants NSC 95-2112-M-001-038-MY2 and NSC 95-2112-M-007-063-MY2.

REFERENCES

Arce, H. G., Shepherd, D., Gueth, F., Lee, C.-F., Bachiller, R., Rosen, A., & Beuther, H. 2007, in Protostars and Planets V, ed. B. Reipurth, D. Jewitt, & K. Keil (Tucson: Univ. Arizona Press), 245
Bachiller, R. 1996, ARA&A, 34, 111
Bachiller, R., & Pérez Gutiérrez, M. 1997, ApJ, 487, L93
Bachiller, R., Pérez Gutiérrez, M., Kumar, M. S. N., & Tafalla, M. 2001, A&A, 372, 899
Bachiller, R., & Tafalla, M. 1999, in The Origin of Stars and Planetary Systems, ed. C. J. Lada & N. D. Kylafis (Dordrecht: Kluwer), 227
Bally, J., Devine, D., & Reipurth, B. 1996, ApJ, 473, L49
Cesaroni, R., Felli, M., Jenness, T., Neri, R., Olmi, L., Robberto, M., Testi, L., & Walmsley, C. M. 1999, A&A, 345, 949
Cesaroni, R., Felli, M., Testi, L., Walmsley, C. M., & Olmi, L. 1997, A&A, 325, 725
Cesaroni, R., Neri, R., Olmi, L., Testi, L., Walmsley, C. M., & Hofner, P. 2005, A&A, 434, 1039
Eislöffel, J., Smith, M. D., Davis, C. J., & Ray, T. P. 1996, AJ, 112, 2086
Fendt, C., & Zinnecker, H. 1998, A&A, 334, 750
Gueth, F., & Guilloteau, S. 1999, A&A, 343, 571
Gueth, F., Guilloteau, S., & Bachiller, R. 1996, A&A, 307, 891
Hatchell, J., Millar, T. J., & Rodgers, S. D. 1998, A&A, 332, 695
Hirano, N., Liu, S.-Y., Shang, H., Ho, P. T. P., Huang, H.-C., Kuan, Y.-J., McCaughrean, M. J., & Zhang, Q. 2006, ApJ, 636, L141
Ho, P. T. P., Moran, J., & Lo, K. Y. 2004, ApJ, 616, L1
Hofner, P., Cesaroni, R., Rodríguez, L. F., & Martí, J. 1999, A&A, 345, L43
Jørgensen, J. K., Hogerheijde, M. R., Blake, G. A., van Dishoeck, E. F., Mundy, L. G., & Schöier, F. L. 2004, A&A, 415, 1021
Kawamura, J. H., Hunter, T. R., Tong, C.-Y. E., Blundell, R., Zhang, Q., Katz, C. A., Papa, D. C, & Sridharan, T. K. 1999, PASP, 111, 1088
Kraus, S., et al. 2006, A&A, 455, 521
Lebrón, M., Beuther, H., Schilke, P., & Stanke, Th. 2006, A&A, 448, 1037
Lee, C.-F., Stone, J. M., Ostriker, E. C., & Mundy, L. G. 2001, ApJ, 557, 429
Moscadelli, L., Cesaroni, R., & Rioja, M. J. 2000, A&A, 360, 663
———. 2005, A&A, 438, 889
Nisini, B., Codella, C., Giannini, T., Santiago Garcia, J., Richer, J. S., Bachiller, R., & Tafalla, M. 2007, A&A, 462, 163
Palau, A., et al. 2006, ApJ, 636, L137
Park, Y.-S., Kim, J., & Minh, Y. C. 1999, ApJ, 520, 223
Raga, A., & Cabrit, S. 1993, A&A, 278, 267
Richer, J. S., Shepherd, D. S., Cabrit, S., Bachiller, R., & Churchwell, E. 2000, in Protostars and Planets IV, ed. V. Mannings, A. P. Boss, & S. S. Russell (Tucson: Univ. Arizona Press), 867
Sault, R. J., Teuben, P. J., & Wright, M. C. H. 1995, in ASP Conf. Ser. 77, Astronomical Data Analysis Software and Systems IV, ed. R. Shaw, H. E. Payne, & J. J. E. Hayes (San Francisco: ASP), 433
Schilke, P., Walmsley, C. M., Pineau des Forets, G., & Flower, D. R. 1997, A&A, 321, 293
Scoville, N. Z., Carlstrom, J. E., Chandler, C. J., Phillips, J. A., Scott, S. L., Tilanus, R. P. J., & Wang, Z. 1993, PASP, 105, 1482
Shepherd, D. S., Yu, K. C., Bally, J., & Testi, L. 2000, ApJ, 535, 833
Shu, F. H., Ruden, S. P., Lada, C. J., & Lizano, S. 1991, ApJ, 370, L31
Sollins, P. K., et al. 2004, ApJ, 616, L35
Su, Y.-N., Zhang, Q., & Lim, J. 2004, ApJ, 604, 258
Tofani, G., Felli, M., Taylor, G. B., & Hunter, T. R. 1995, A&AS, 112, 299
Viti, S., & Williams, D. A. 1999a, MNRAS, 305, 755
———. 1999b, MNRAS, 310, 517
Wilson, T. L., & Rood, R. T. 1994, ARA&A, 32, 191
Wood, D. O. S., & Churchwell, E. 1989, ApJ, 340, 265
Zhang, Q., Hunter, T. R., Sridharan, T. K., & Cesaroni, R. 1999, ApJ, 527, L117
Ziurys, L. M., Friberg, P., & Irvine, W. M. 1989, ApJ, 343, 201